

Cover Page



Universiteit Leiden



The handle <http://hdl.handle.net/1887/138674> holds various files of this Leiden University dissertation.

Author: Vlieg, R.C.

Title: Two-photon multifocal microscopy for in vivo single-molecule and single-particle imaging

Issue Date: 2020-12-14

Chapter 2

Multiplexed two-photon excitation spectroscopy of single gold nanorods

Plasmonic metallic nanoparticles are commonly used in (bio-)sensing applications because their localized surface plasmon resonance (SPR) is highly sensitive to changes in the environment. Although optical detection of scattered light from single particles provides a straightforward means of detection, the two-photon luminescence (TPL) of single gold nanorods (GNRs) has the potential to increase the sensitivity due to the large anti-Stokes shift and the non-linear excitation mechanism. However, two-photon microscopy and spectroscopy are restricted in bandwidth and have been limited by the thermal stability of GNRs. Here we used a scanning multifocal microscope to simultaneously measure the two-photon excitation spectra of hundreds of individual GNRs with sub-nanometer accuracy. By keeping the excitation power under the melting threshold, we show that GNRs were stable in intensity and spectrum for more than 30 min, demonstrating absence of thermal reshaping. Spectra featured a signal-to-noise ratio > 10 and a reduced plasmon peak width of typically 30 nm. Changes in the refractive index of the medium of less than 0.04, corresponding to a change in surface plasmon resonance of 8 nm, could be readily measured and over longer periods. We used this enhanced spectral sensitivity to measure the presence of neutravidin, demonstrating the potential of TPL spectroscopy of single GNRs for enhanced plasmonic sensing.

Vlieg, R. C., Pham, C., van Noort, J. Multiplexed two-photon excitation spectroscopy of single gold nanorods. *In preparation*.

2.1 INTRODUCTION

The unique optical properties gold nanorods (GNRs) have raised interest of multiple fields of research and industry. A weak plasmon-induced optical luminescence signal of bulk gold was first reported by Mooradian¹. Mohamed et al. later observed that the luminescence of gold could be enhanced by $>10^6$ when exciting rod-shaped gold nanoparticles in resonance with their surface plasmon wavelength, typically in the near-infrared (NIR) part of the spectrum, increasing the quantum yield to $\sim 10^{-4}$ ². This field enhancement yields a signal intensity similar to that of quantum dots³, being bright enough for straight-forward detection of individual particles. GNRs however, do not blink and gold provides excellent biocompatibility, making them more appealing for biological applications. In combination with the reduced absorbance and scattering of NIR light *in vivo*, GNRs form attractive labels for *in vivo* imaging^{3,4}, but GNRs are also used in cancer therapy, fluorescence enhancement and bio-sensing⁵⁻¹².

The longitudinal SPR wavelength of a GNR is almost independent of the rod diameter for diameters < 50 nm, but scales linearly with its aspect ratio¹³, yielding resonances between 600 and 1000 nm for aspect ratios between 2 and 5. Because the electric field of the GNR is confined to several 10's of nanometers from the tips of the GNR¹⁴, it creates a very local excitation volume, down to several zeptoliter, which can be readily exploited for single-molecule biosensors, even in high concentration solutions^{8,15-17}. The distinctive merits of single-molecule detection, i.e. avoiding population and temporal averaging, provide an attractive new range of applications of GNRs, but have to date mainly been demonstrated as proof-of-principle studies, lacking sufficient throughput and bandwidth for widespread exploitation.

Metallic nanoparticles can be used for (bio-)sensing in two manners, as reviewed by Taylor, et al.¹⁸. First, the intensity of fluorescently labeled analytes is highly enhanced when entering the proximity of the nanoparticle by increases of both the excitation rate and the quantum yield of the fluorophore. This fluorescence enhancement requires sufficient spectral overlap between the plasmon and the spectrum of the label. Various examples of single-molecule detection have been reported^{15,19}. When labeling of analytes is not desired, GNRs can also be used as label-free detectors. In this mode, a change in the dielectric properties of the surroundings, as analytes enter the proximity of a GNR²⁰⁻²², induces a shift in the plasmon resonance. This plasmon shift can amount up to several nanometers, but is highly dependent on the nanoparticle geometry, binding position and size of the analyte.

Fluorescence enhancement and SPR shifts can readily be measured in bulk²³. However, bulk analysis yields the average properties of a potentially complex solution and the kinetics can only be extracted indirectly. In the case of GNRs, the measured signal is further convoluted by the poly-dispersity of the particles. Though GNRs can be synthesized with fairly small poly-dispersity¹³, the strong geometry-dependence of the SPR compared to its linewidth typically broadens the bulk spectrum as compared to single GNRs. Optimal sensitivity therefore requires analysis of individual GNRs, rather than bulk-averaged signals.

Microscopic techniques provide access to spectroscopic properties of individual GNRs, sparsely distributed on a transparent substrate. Optical signals from GNRs can be divided into

scattering, one-photon luminescence, photo-thermal scattering, and two-photon luminescence. GNRs have a high-scattering cross-section and detection can straightforwardly be multiplexed by wide-field imaging using dark-field excitation¹⁹. Scattering from other sources than GNRs may be difficult to discriminate in complex environments, limiting the sensing applications to relatively clean samples. Confocal imaging provides better rejection of undesired scattering, at the cost of lower throughput. Because the illumination beam focusses on a single GNR at a time, spectrometric analysis can easily be introduced in the emission path of the microscope, resolving both the transversal SPR at ~ 500 nm and the longitudinal SPR at NIR wavelengths^{24,25}. As particles get smaller, the absorption cross-section becomes dominant over the scattering cross-section. One-photon luminescence is based on detecting the photons that are emitted after radiative relaxation of optically excited GNRs^{25,26}. The associated Stokes shift of the emitted light allows for spectral filtering of luminescence from scattering. Next to radiative relaxation there is non-radiative relaxation which results in heating of the GNR. This is exploited in photo-thermal imaging, in which the increased scattering induced by the elevated refraction index of the medium surrounding the GNR, is detected through second non-resonant laser beam¹⁵. In this chapter we will focus however on two-photon luminescence of single GNRs, which will be further discussed below. Next to detailed insight into their geometry and fundamental photo-physical properties, spectroscopic analysis of single GNRs also is key to design sensors with desired sensitivity and kinetic response¹⁸.

The potential of spectroscopy two-photon luminescence (TPL) of GNRs for sensing applications has yet to be explored. TPL results from successive absorption of two photons, and subsequent rapid radiative decay, which is strongly enhanced in nano particles relative to bulk gold. The quadratic dependence of the TPL signal on excitation power produces sharper plasmon resonance peaks compared to single-photon microscopy. Wang et al. for example measured TPL intensity of single GNRs with a fixed excitation wavelength of 820 nm, which indeed resulted in a narrower linewidth of the SPR compared to the bulk absorption spectrum³. Zijlstra et al. and Molinaro et al. also showed TPL excitation spectra of a single GNR^{27,28}. However, these spectral measurements were rather limited in both sample size and spectral resolution, due to manual laser tuning and the confocal nature of typical two-photon setups.

Another major obstruction for using TPL of GNRs in sensing applications is their limited thermal stability²⁹⁻³⁴. As exploited by photo-thermal imaging, on-resonance excitation leads to heating of GNRs, which can result in temperature increases of 10s to 100s of degrees²⁹. Thermally induced diffusion of surface atoms, which happens at temperatures far below the bulk melting temperature of gold, reduces the aspect ratio of GNRs and therefore drastically changes the longitudinal plasmon resonance³⁴. The high-intensity pulsed laser excitation required for TPL results in reshaping at powers of several mJ/cm². Next-to stability of the optical signal, elevated temperatures are also detrimental for the stability of the biomolecules, so reduction of photothermal effects in TPL is crucial for biological applications.

Here we present wide-field two-photon spectroscopy of single GNRs, using an automated tunable Ti:Sa laser in combination with a multifocal microscope. Scanning an area of 60 by 60 μm with 625 focused laser beams at framerate of several frames per second yielded rapid, high signal-to-noise, multiplexed optical detection of hundreds of GNRs. By tuning the excitation wavelength, we measured individual TPL excitation spectra and showed that these were stable

for 10s of minutes. Finally, we resolved changes in the refractive index of the surrounding medium similar to those expected from single-molecules to illustrate the potential of TPL of GNRs for bio-sensing applications.

2.2 MATERIALS AND METHODS

Microscopy setup. A tunable near-IR Ti:Sa laser (Coherent, Chameleon Ultra) was coupled into a home-build two-photon multifocal microscope, depicted in Figure 2.1a. A diffractive optical element (DOE, custom made by Holo-eye) diffracted the laser beam into an array of 25x25 foci. A fast-scanning mirror (Newport, FSM-300-1) driven by an Archimedean spiral rapidly scanned the beams yielding a fairly homogeneous wide-field illumination, as characterized before⁴. The laser beams were focused using a 60X NA 1.49 TIRF objective (Nikon, CFI Apochromat TIRF 60XC Oil), illuminating area of 60x60 μm^2 , shown in Figure 2.1b. A single period of the spiral scan took 100 ms and was synchronized with the image integration time. Based on the scan pattern and point spread function, we estimate the duty cycle for illumination of a single location in the sample to be around 2%. The wavelength for excitation was automatically tuned over the range of 720 - 950 nm. Polarization of the excitation light was controlled by inserting a half wave plate (Thorlabs, AHWP05M-980) mounted stepper-motor stage. For circularly polarized light the quarter wave plate was removed and only a quarter wave plate (Thorlabs, AQWP05M-980) was included. TPL was collected by the same objective, filtered with a dichroic mirror (Semrock, 700dcxr) and a 720 nm short pass filter (Semrock, FF01-720-SP) and focused on a 512x512 pixel EM-CCD camera (Photometrics, QuantEM 512SC). Using self-written LabVIEW (National Instruments) software, the laser, scanning mirror, stepper motor and camera were controlled in synchrony, to record time traces in which either polarization or wavelength were scanned, see Figure 2.1c. For measurements in which the refractive index of the medium was varied and for neutravidin-sensing, we used a 25X NA 1.1 water dipping objective (Nikon, CFI75 Apochromat 25XC W) and a back-illuminated 2048x2048 sCMOS camera (Photometrics, PRIME BSI), resulting in a 145x145 μm^2 field of view.

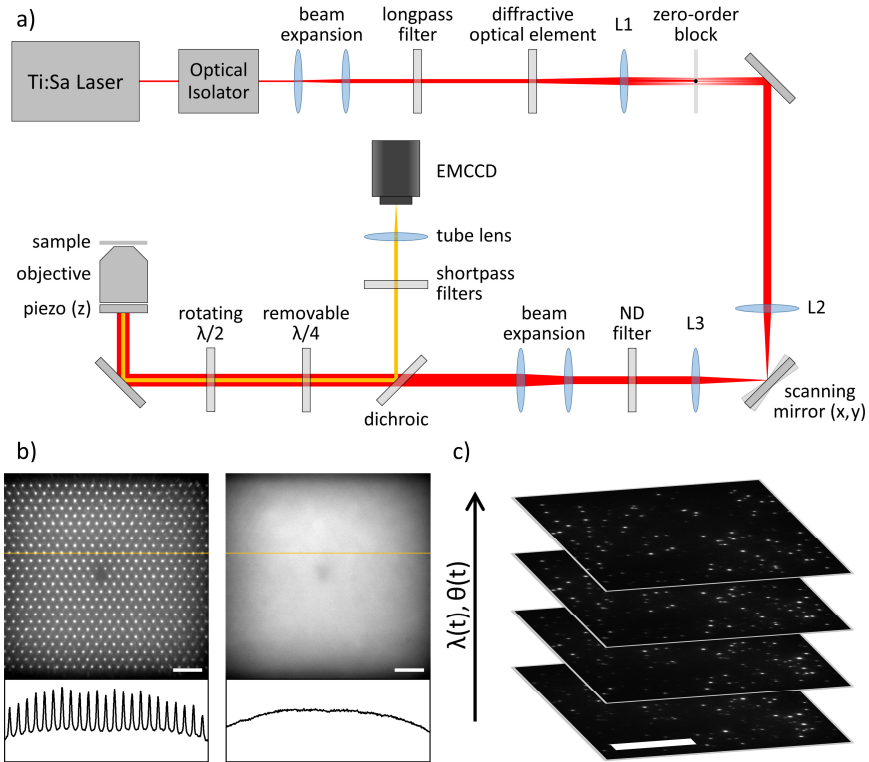


Figure 2.1: Multifocal two-photon laser scanning microscopy setup for high-throughput microscopy and spectroscopy. (a) Schematic overview of the setup. The laser beam is diffracted in an array of 25×25 foci by a diffractive optical element (DOE). (b) A wide-field excitation pattern is generated by spiral scanning the DOE pattern within the exposure time of the camera. (c) A stack of 2D images of GNRs dispersed on a glass slide. The polarization (θ) and wavelength (λ) are changed per slice, resulting in spectral characterization of the GNRs. Scale bar = 30 μm .

Sample preparation. Glass coverslips were rinsed with ethanol and dried in a stream of nitrogen. 10 μm microliter of GNRs (Nanopartz, A12-10-808) diluted in 100 μl of distilled water and were spin-coated in three steps: 200 rpm for 5 seconds, 600 rpm for 15 seconds and 1000 rpm for 60 seconds. After deposition, the samples were treated in an UV-cleaner (model No. 42A-220, Jelight company) for 30 minutes.

Data analysis. High intensity peaks in the images were attributed to single (clusters of) GNRs. Regions of interest of 5×5 pixels around each peak were summed and background subtracted, yielding TPL signal I . TPL intensity as a function of the excitation wavelength λ was fitted to a squared Lorentzian:

$$I(\lambda) = \frac{I_0}{\left(1 + 4(\sqrt{2} - 1) \left(\frac{\lambda - \lambda_{\text{SPR}}}{\omega}\right)^2\right)^2 + C} \quad (2.1)$$

where λ_{SPR} is the SPR, ω the Full Width at Half Maximum of the SPR, I_0 the maximum intensity, and C an offset corresponding to residual background signal.

TPL signal as a function of the polarization angle of the excitation light θ was fitted to:

$$I(\theta) = I_0 \cos^4(\theta + \theta_0) + C \quad (2.2)$$

with θ_0 being the orientation of the GNR relative to the polarization angle of the laser.

Scanning Electron Microscopy. For scanning electron microscopy (SEM) measurements, GNRs were spin-coated on an indium tin oxide (ITO) coated cover glass (SPI Supplies, 06480-AB), following the same cleaning and deposition procedure as for regular slides. Using a diamond tipped pen, a cross was scratched in the glass surface to provide a reference point for correlating the two microscopy modalities. The sample was first imaged in the two-photon microscope, after which it was placed in the SEM (FEI, Nova NanoSEM).

Sucrose solutions. Sucrose solutions in HPLC grade water were used to control the refractive index of the medium. The refractive index of each sucrose solution was measured using a refractometer (Carl-Zeiss). To facilitate exchange of solutions, measurements were performed in flow cells made from two glass coverslips that sandwiched a piece of double sided tape with cut out flow channels into which fluids were pipetted.

Neutravidin detection. Neutravidin sensing measurements were performed in similar flow cells as the sucrose experiments. One-step passivation of the glass coverslip was performed, following the protocol of Gidi et al. with a few modifications³⁵. Glass coverslips were cleaned with an UVO cleaner for 10 minutes. After UVO treatment, coverslips were put in a petri dish containing desiccant (i.e. calcium chloride) and pre-heated in an oven at 90 °C for 5-10 minutes to further ensure water-free conditions. To graft the silane PEG azide (SPA) on the coverslip's surface, 1 ml of 0.1% SPA in anhydrous DMSO solution was evenly spread on the coverslip's surface and heated at 90 °C for 30 minutes. Coverslips were rinsed with 1 ml HPLC grade water and dried under a continuous stream of N₂ to remove excess SPA. After which the flow cells were assembled.

Four oligo sequences were purchased (Intergrated DNA Technologies, USA), of which the specific sequences can be found in Table 2.1. All oligo's were prepared in Tris buffer (pH =7.2).

Oligo sequence #	Sequence & base pair (bp) length
OS1	/5DBCOTEG/AAATTATAACTATTCCTA (18 bp)
OS2	TAGGAATAGTTATAAAAA/3DTPA/ (18 bp)
OS3	GGTGGTGGTGGTTGTGGTGGTGGTGAAAAA/3DTPA/ (35 bp)
OS4	ACCACCACCACAAA/3Bio/ (15 bp)

Table 2.1: The sequences of the oligo's used for the neutravidin sensing experiments.

GNRs (Nanopartz, A12-10-808) were conjugated with OS2 and OS3, following a conjugation protocol from J. Li, et al.³⁶. In short, GNRs were mixed with 0.02% sodium dodecyl sulfonate (SDS), 1x tris-borate-EDTA (TBE) and 500 mM NaCl (pH=3.5). Oligo OS2 and OS3 were added with a 1:1000 GNRs-oligo ratio and the whole mixture was incubated for 30 minutes mounted on a rotator at room temperature. SDS screens the positive charge of the CTAB and assist in the functionalization of the GNRs with the thiolated oligo's. The GNR-oligo pellets were separated from the supernatant by centrifuging at 8000 rpm for 30 minutes. The GNR-oligo was reconstituted in the Tris buffer and stored at 4 °C for future use.

50 μ l of oligo OS1 [3.33 μ M] was incubated in the channels of the flow cells for 1 hour at the room temperature to allow the copper free Click Chemistry of DBCO and azide. The DBCO at 5' end of the oligo covalently binds to the azide of the SPA grafted on the coverslip's surface. Next, the flow cells were incubated with 50 μ l of the GNR-oligo OS2, OS3 solution for further 15-30 minutes to allow the annealing of oligo OS1 and OS2. After that, the flow cells were rinsed with 200 μ l Tris buffer. The flow cells were either subsequently used or stored at 4 °C for future experiments.

Neutravidin was mixed with oligo OS4 at a ratio of 1:4 in Tris buffer (pH=7.2). Oligo OS4 was annealed with oligo OS 3 on the GNRs and the biotin at 3' end of the oligo was conjugated with the neutravidin (a final concentration of 25 nM). The samples were ready for the measurement.

The average of the selected time traces was normalized (I_{norm}) and weighted according to:

$$I_{norm}(t) = \frac{\sum_n (I_n(t) * s_n)}{\sum_n |s_n|} \quad (2.3)$$

where $I_n(t)$ is the signal intensity at time t for trace n and s_n the sensitivity of trace n at the excitation wavelength as measured from the excitation spectra prior to the time trace measurement.

The standard deviation of the normalized intensity SD_{norm} was defined according to:

$$SD_{norm}(t) = \frac{\sum_n ((I_n(t))^2 - \bar{I}(t)^2) * s_n}{\sum_n s_n^2} \quad (2.4)$$

where the signal per trace I_n at time t is subtracted by the average signal of all selected traces \bar{I} at time t .

2.3 RESULTS

To identify and characterize the TPL signal of single GNRs, we first compared TPL imaging with scanning electron microscopy (SEM) images. SEM readily showed the location, geometry and orientation of single GNRs. Figures 2.2a and 2.2b show that the positions of the GNRs as identified by SEM and TPL imaging are highly correlated. The orientation of individual rods was confirmed by TLS imaging as a function of the polarization angle of the excitation beams. The corresponding polarization spectra, an example is shown in Figure 2.2c, follow eq. 2.2 and readily resolve the orientation of each rod with a standard error of fit of less than 1 degree. Differences between the orientation as obtained by TPL and from the SEM images were within 10 degrees and may originate from optical aberrations in the excitation and/or imaging path. Nevertheless, the good agreement between the SEM and TPL imaging confirms that indeed single GNRs can be identified using TPL, and that successive wide-field two-photon imaging can accurately resolve the orientation of these.

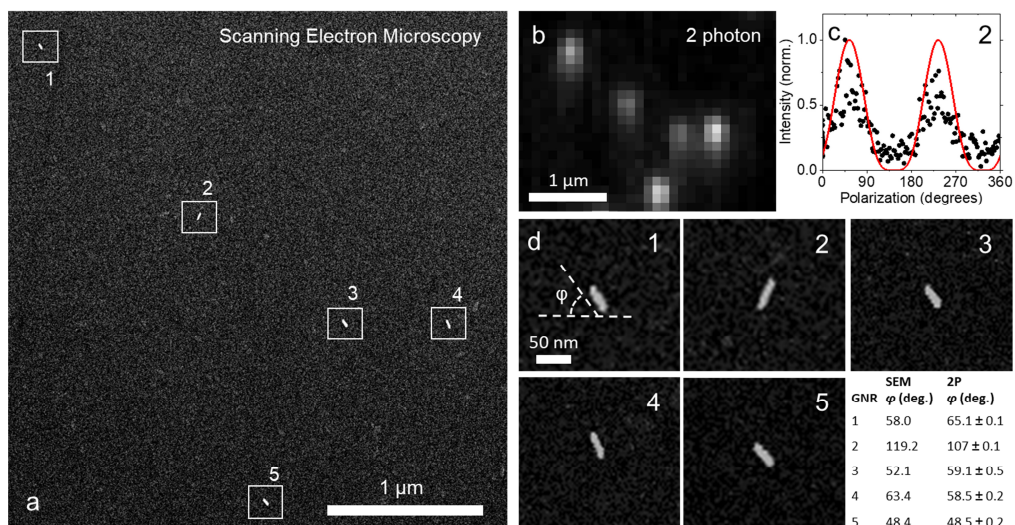


Figure 2.2: Correlated light and electron microscopy (CLEM) of single gold nanorods. (a) Scanning electron microscopy image of single GNRs dispersed on an ITO-coated glass substrate. (b) Two-photon image of the same GNRs as in (a). (c) Orientation of the rods in two-photon microscopy is measured by rotating the polarization of the linear excitation light. (d) GNR close-ups from the electron microscopy image. The orientation of the GNRs is determined by fitting an ellipsoid.

Similar to obtaining polarization spectra, we measured excitation TPL spectra of single GNRs in wide-field by scanning the excitation wavelength from 730 to 900 nm in successive images. Figure 2.3a shows the TPL image of a typical field of view of GNRs deposited on a glass coverslip and immersed in water. The background-corrected signal intensity of the GNRs varied between 9 and 140 kHz. Intensity can however not be used to identify single GNRs as differences in intensity can arise from different sizes of the GNRs or from diverse aspect ratios

which lead to different excitation efficiency when exciting at a fixed wavelength. Moreover, clusters of multiple GNRs may result in a single diffraction limited spot that cannot be differentiated from a single GNR based on size. The excitation spectra however, were more informative. The TPL excitation spectra of six GNRs are plotted in Figure 2.3b. Spectra were fitted to a squared Lorentzian (eq. 2.1) which is characteristic for two-photon excitation. The spectrum of area 4 however, showed two distinctive peaks and better matched product of two squared Lorentzians, suggesting two GNRs in a single spot. Figure 2.3c and d show the results of fitting TPE spectra of hundreds of GNRs measured in three field-of-views. All fits to eq. 2.1 with an r-squared value larger than 0.6 were included in the analysis. The distribution of SPRs in this population of GNRs varied in the range of 730-850 nm, largely resembling the bulk absorption spectrum, though SPR dropped more rapidly after 825 nm in single GNR measurements. This probably reflects the reduced intensity of our laser at larger wavelength. The power spectrum of the laser is plotted for reference in supplementary figure S2.1. Figure 2.4b shows the width of the TPE spectra of 478 single GNRs, yielded a Full-Width-at-Half-Maximum of 31 ± 1 nm (mean \pm sd). The very narrow distribution not only reflects the very homogeneous optical properties of the batch of GNRs, it also demonstrates the accuracy of TPL excitation spectroscopy using scanning multifocal microscopy.

For bio-sensing applications, it is important that the SPR of single GNRs is stable over time. Absorption of intense femtosecond pulses can lead to heat-induced reshaping of the GNR, resulting in a blue-shift of the spectrum. We mapped the stability of GNRs during continuous spectral measurements by sweeping the excitation wavelength between the range of 730 and 850 nm every 25 seconds. Figure 2.4a shows the changes in excitation spectrum of a GNR with a laser power of 4.1 mW. We observed reshaping of the GNR from 780.7 nm to 755.0 nm at a rate of 2.3 nm per sweep. At a power of 1.6 mW ($2.56 \mu\text{W}/\text{focus}$) however, the spectrum was quite stable, as shown in Figure 2.4b. At the start of the measurement we fitted the SPR at 766.4 nm. The last spectrum, after 216 measurements, yielded an SPR at 766.8 nm, indicating the absence of reshaping. We estimate this laser power to be equivalent to approximately 31 fJ per pulse. Indeed, this laser power is below the reported damage threshold of 60fJ^1 , demonstrating that at sufficiently low excitation power two-photon excitation does not affect the stability of a GNR.

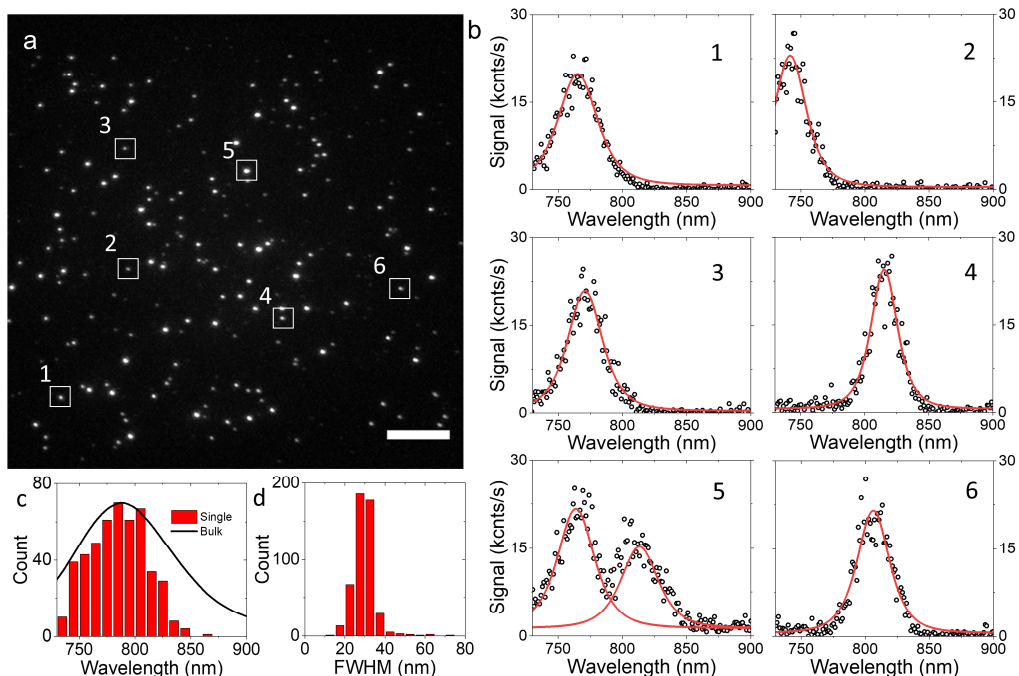


Figure 2.3: Multiplexed two-photon spectroscopy reveals excitation spectra of individual GNRs. (a) The spectra are acquired in parallel within the field of view of the camera. (b) Spectra of single rods are fitted to a squared Lorentzian (eq. 2.1). The spectrum of GNR 4 is fitted to two squared Lorentzians. (c) The distribution of SPRs measured in multiple field-of-views compared to the bulk spectrum. (d) The FWHM of the two-photon spectra shows an average width of 31 nm. Parameters are acquired from fitting eq. 2.1 to the raw data. Scale bar = 10 μm .

The trends observed in these two GNRs were representative of most GNRs. Figure 2.4c shows the spectral drift of 4 other GNRs as well as the average trend for 49 GNRs. Differences in reshaping rate probably reflect differences in GNR size, as larger GNRs will heat faster due to a larger absorption cross-section. The SPR stabilized around 725 nm. This probably reflects the reduced laser power at smaller wavelengths. At 1.6 mW, all spectra remained largely stable, as shown in Figure 2.4d. Only in the first wavelength-sweep, did we observe a small shift for some GNRs, which we tentatively attribute to laser induced changes in the immediate surrounding of the GNRs, rather than reshaping of the GNR itself. In any case, the spectrum of individual GNRs was stable for tens of minutes, opening the way for GNR based label-free sensing applications using TPL.

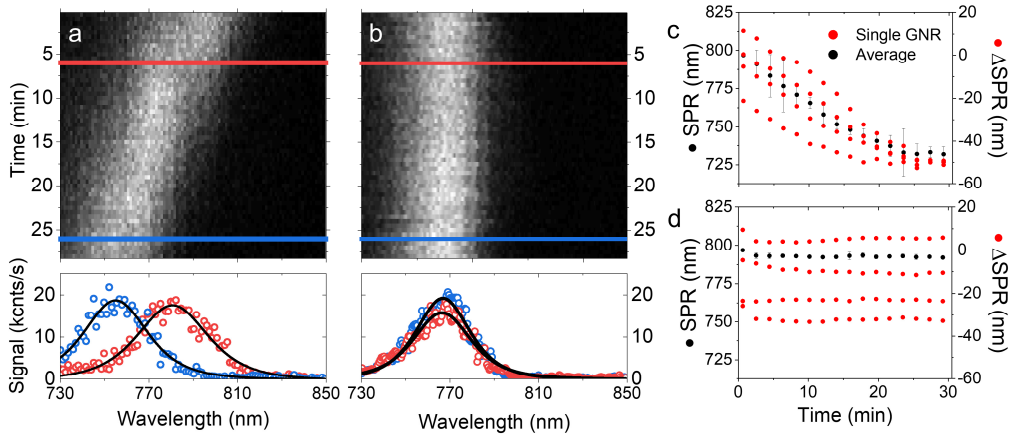


Figure 2.4: Gold nanorods remain stable during nearly 30 minutes of two-photon excitation. (a) Spectrogram of one GNR as the excitation wavelength is continuously swept back and forth during the measurement. The bottom graph shows the spectrum at the start of the measurement (red) and at the end (blue). (b) Spectrograph and corresponding graph of a single GNR when laser power is reduced by 40% to ± 31 fJ. The SPR remains within 1 nm of the SPR measured at the start of the measurement. (c) The SPRs of multiple rods with the laser power at ± 75 fJ per pulse. Single rods are depicted in red and the average in black. (d) SPRs of multiple rods with lower excitation power.

To demonstrate the sensitivity of TPL spectroscopy on single GNRs, we measured their spectral response when changing the refractive index of the medium from that of water ($n=1.333$) to two different sucrose solutions. The bulk spectrum, as plotted in Figure 2.5a, red-shifted by 12 and 14 nm when the refractive index increased from 1.333 to 1.376 and subsequently to 1.432. This spectral shift corresponds to a sensitivity of 255 nm/refractive index unit (RUI) for this batch of GNRs. The TPL spectra of single GNRs showed a similar trend as plotted in Figure 2.5b and c. By only comparing the shift, we obtained a narrow distribution of changes in SPR for a large population of GNRs. A shift 8 ± 3 nm was observed when going from $n = 1.333$ to $n = 1.376$, 12 ± 7 nm when changing from $n = 1.376$ to $n = 1.432$, and 21 ± 8 nm when the medium was changed from $n = 1.333$ to $n = 1.432$. The change in SPR was reversible as changing the medium back from $n = 1.432$ to $n = 1.333$ reduced the SPR by -26 ± 9 nm. Despite that the SPR varied over more than 80 nm between GNRs, the shift of individual GNRs was very reproducible. In Figure 2.5e the SPRs for a number of GNRs are plotted as a function of the refractive index of the medium. The majority of the GNRs showed a linear increase in their SPR, though some deviated slightly from the linear trend. The slope is independent from the location of the SPR. The average change in SPR was proportional with Δn , as shown in figure 2.5d and yielded a slope 237 ± 9 nm per refractive index unit, in fair agreement with the bulk value.

2.3 Results

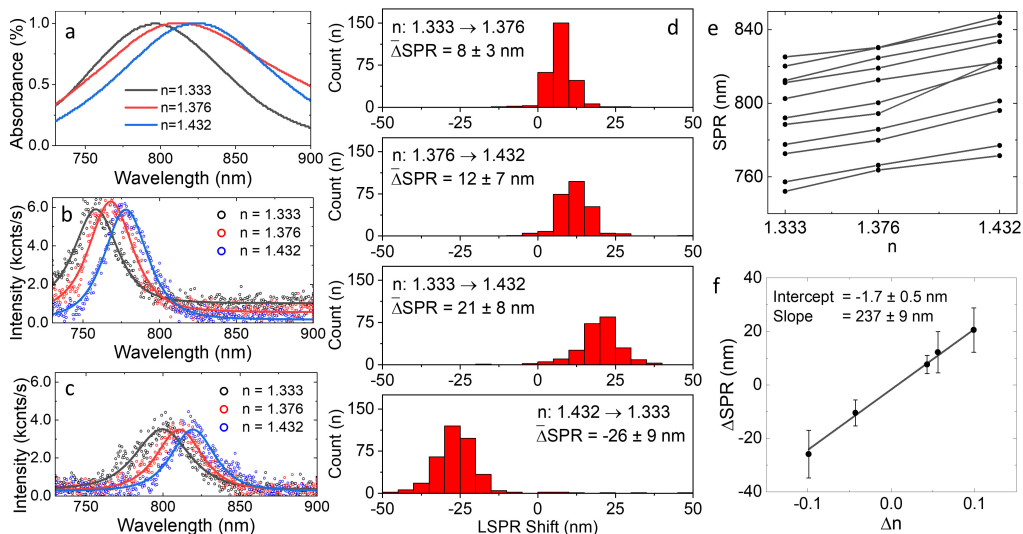


Figure 2.5: The LSPR shift of individual gold nanorods is resolved by two-photon spectroscopy. (a) UV-VIS spectra of bulk solutions of GNRs in: water, 30% sucrose and 70% sucrose solutions, respectively. (b,c) The spectrum of a GNR in water and the two different solutions of sucrose. Both rods show a red-shift when the refractive index is increased. (d) The $\bar{\Delta}$ SPR of single GNRs when changing the refractive index of the medium. (e) The SPRs of individual GNRs as it shifts with different refractive indexes. (f) The $\bar{\Delta}$ SPR as it is plotted against the change in refractive index. The data is fitted to a linear function.

Next we ventured towards single-molecule sensing experiments. Prior to the measurement, GNRs were functionalized with two types of oligo's. One oligo sequence (OS) for immobilization of the GNR on the glass and another for specific and long-lasting binding to analytes featuring a third complementary OS, see Figure 2.6a. After GNRs were immobilized on the glass surface, the excitation spectrum was measured by sweeping the laser from 730 nm to 900 nm while taking consecutive images. SPR peaks of the rods were fitted to a 2D Gaussian, and the corresponding amplitudes were used to produce an excitation spectrum for every rod in the FOV. The laser power was increased to 3.0 mW to improve SNR at a trade-off of rod stability. We found that most of the rods were stable and were suitable for sensing experiments. Once the excitation spectra were acquired, the wavelength was fixed at 800 nm and the luminescence of each GNR was measured continuously. A solution containing 25 nM neutravidin-oligo complex was flushed in the flow cell after 120 seconds of imaging. The complementary sequences of OS3 and OS4 allowed for specific binding of the neutravidin to the GNRs. After 380 seconds, a second excitation spectrum was taken to assess SPR shifts. The excitation spectra were fitted to a Lorentzian squared (eq. 2.1). All spectra with a FWHM larger than 35 nm were discarded from further processing to exclude GNR clusters from the data. After selection, the measurement yielded 82 traces. A control measurement, where only buffer was flushed in the flowcells, yielded 73 traces.

Figure 2.6b shows the TPL spectra of a rod before and after neutravidin was added to the medium. The SPR was red-shifted by 15 ± 1 nm, indicating an increase of the local refractive index. The initial sensitivity of the GNR is around 25 photons/sec/nm based on the derivative

of the fitted Lorentzian squared. Note that the sensitivity increases to 50 photons/sec/nm when the SPR red-shifts, as the rod is excited at a steeper part of its SPR spectrum. In Figure 2.6c, the signal intensity remained relatively stable during the first 120 seconds of the measurement. Upon flushing-in oligo-neutravidin solution, the signal intensity increased, which we attribute to a red-shift of the SPR. Discrete steps of approximately 212 photons/sec can be discerned in the time trace. Based on the sensitivity corresponds to a 15 nm red shift of the SPR. For such a large change, it is more plausible that multiple neutravidin molecules bind to the GNR. The signal intensity decreased after 320 seconds, suggesting that the rod reshaped when excited at a higher absorption cross section. However, the spectrum that was measured afterwards showed a red-shifted peak, relative to the original spectrum, suggesting that desorption may also have happened.

A similar response was seen for the rod in Figure 2.6d and e. Initial signal intensity of the time trace is 1019 ± 227 photons/sec. It decreased instantly to 357 ± 164 photons/sec after addition of neutravidin, suggesting multiple binding events. The decrease in signal intensity is conform with the location of the SPR peak relative to the excitation wavelength. More examples of spectra and time traces resembling the ones shown here are plotted in Figure S2.2.

We flushed-in buffer absent of oligo-neutravidin to verify that the SPR perturbations are not caused by proteins and measurement artefacts like instabilities or buffer impurities. The spectra of one GNR from this control measurement, plotted in Figure 2.6f, show that the SPR shifted marginally, by 0.4 ± 0.5 nm, upon flushing in buffer. The time trace of the corresponding GNR, shown in Figure 2.6g, continues as a constant signal intensity. The spectra and time traces plotted in Figure S2.3 illustrate similar behavior of other GNRs measured in this control experiment.

2.3 Results

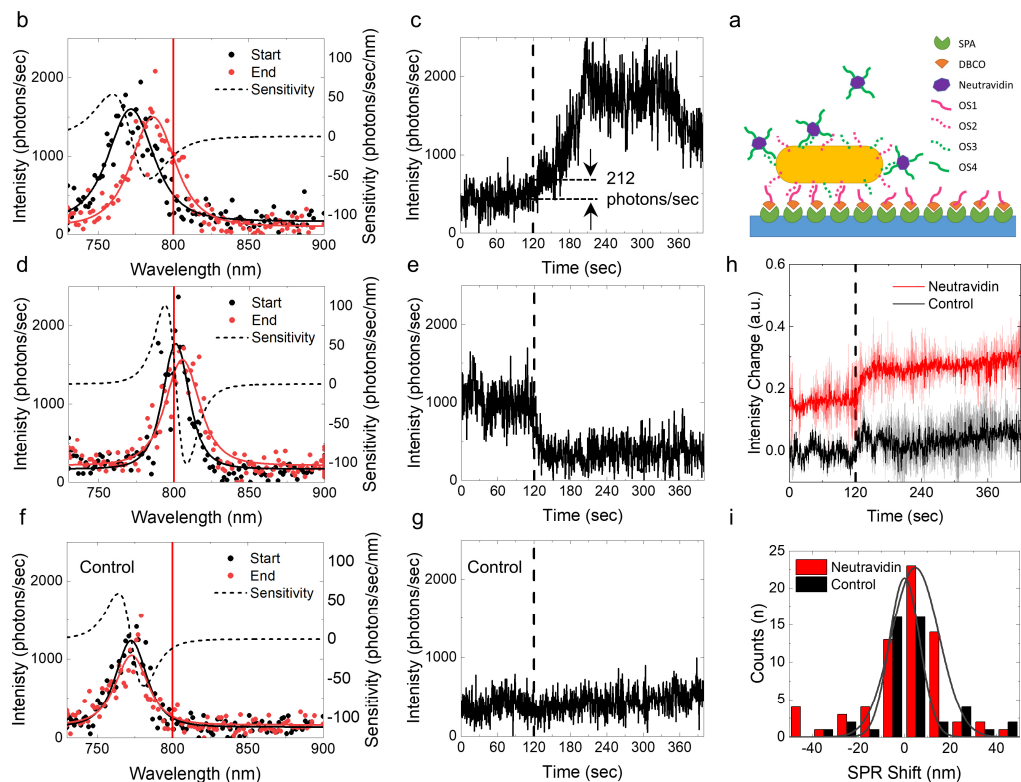


Figure 2.6: Specific binding of DNA oligo-neutravidin complexes induce a shift in the LSPR. (a) Schematic of the experiment. Inside a flow cell, GNRs are immobilized on a glass surface by binding of two complementary oligo strands (pink). A second oligo pair (green) mediates binding of neutravidin to the GNR. (b,d) Excitation spectra of two GNRs before (black) and after (red) addition of neutravidin to the medium. In both instances the LSPR is red-shifted, indicating an increase of the refractive index of the medium surrounding the rod. The data is fitted to a squared Lorentzian (solid lines) according to eq. 2.1. The derivative of the fitted curve (dotted line) indicates the expected signal change upon a shift in the LSPR. Both rods were excited at 800 nm (vertical red line). (c,e) Time traces of the GNRs corresponding to the spectra in the column of b. After 120 seconds of imaging (dotted black line), 25 nM neutravidin was flushed in the flowcell, resulting in signal intensity changes. (f,g) The excitation spectra and time trace of a GNR where buffer, instead of neutravidin, was flushed in after 120 seconds of imaging. No LSPR shift was observed and the time trace did not feature significant changes in signal intensity. (h) Normalized and weighted average signal intensity, according to eq. 2.3, of the ensemble of GNRs when flushing in neutravidin (red) or only buffer (black) at 120 seconds (dotted black line). The red trace is offset for clarity, and started at zero. (i) The SPR shift of the ensemble of GNRs. When neutravidin was added the LSPR features an average red shift of 5 ± 1 nm.

To quantify the response of all rods we averaged and weighted the time signals according to eq. 2.3 and plotted the results in Figure 2.6h. The average signal intensity changed $12 \pm 4\%$ with the addition of neutravidin. Flushing-in buffer absent of neutravidin resulted in a shift of $4 \pm 2\%$. The larger average intensity change when adding neutravidin indicates a specific response. The standard deviation (SD), defined in eq. 2.4, of both averages also increases after 120 seconds. This could be caused by mechanical instabilities, impurities in the solution or reshaping of the GNRs, which would also explain the relative wide distribution of the SPR shift

in Figure 2.5i. By fitting a Gaussian function to the distribution of SPR shifts, we find that the SPR shifts during the control measurement on average 0.1 ± 0.8 nm, with a FWHM = 16 ± 3 nm. Note that the SPR is both red- and blue -shifted without a specific direction, as is also seen in the averaged time trace and depends on the initial position of the SPR relative to the excitation wavelength. The average SPR of the GNRs with oligo-neutravidin was a red-shifted by 5 ± 1 nm, which matches the trend we saw in the average time trace in Figure 2.6h, and confirms a specific interaction of oligo-neutravidin with the GNR.

2.4 DISCUSSION AND CONCLUSION

We measured the TPE spectra of single GNRs in parallel by scanning the excitation wavelength of a multi focal two-photon microscope. The narrow peaks of the plasmon resonances follow a squared Lorentzian dependence, which confirms two photon excitation. Irradiation of rods with an energy estimated at 31 fJ per pulse allowed for stable spectra measurements for nearly 30 minutes. Whereas increasing excitation power to above the threshold level resulted in reshaping accompanied by a blue-shift of the plasmon resonance. We demonstrated that by changing the refractive index of the medium the TPE spectra shifted accordingly. We observed specific interactions of oligo-functionalized GNRs with complementary oligo-neutravidin molecules in solution.

To identify TPL from single GNRs we correlated SEM with two-photon images. Besides SEM, single GNRs were also identified by making use of light polarization and the excitation spectra. Considering the spectra measurements, as shown in Figure 2.3b, clusters of GNRs resulted in a broader SPR because the spectrum is the product of multiple individual rods combined. Previous studies also concluded that the spectrum of a cluster of rods is a combination of multiple single GNRs³⁷⁻³⁹. Discriminating single GNRs from clusters by using light polarization was used as an alternative method. The $\cos^4(\phi)$ dependence on polarization seen in Figure 2.1 for a single rod agrees with earlier findings H. Wang et al. and K. Imura et al., which furthermore confirms that the collected signal originates from a two-photon excitation process^{3,40}.

The plasmon resonance for single GNRs was determined with sub-nanometer accuracy. The average FWHM we found is $\pm 35\%$ smaller compared to reported one-photon spectra which lies approximately between 45 and 60 nm^{6,17,41,42}. Moreover, the width of 24 nm for the narrowest peaks is nearly a factor of two smaller than any reported one-photon spectra we could find. Narrow peaks are preferred for sensing applications as narrower peaks translate to a larger derivative around the SPR and therefore higher sensitivity. We attribute differences in FWHM to inhomogeneity's in the ensemble of GNRs as the width of the plasmon resonance depends on the volume of the rod⁴³.

TPE spectra from previous studies, although limited in their bandwidth, do provide details about FWHM. Zijlstra et al. measured a reduction in FWHM of approximately 60% when comparing scattering- or one-photon luminescence- to TPE spectra²⁷. C. Molinaro et al. showed

that their measured TPE spectra overlaps with the model of absorption calculated using Gans-Mie theory, which describes the scattering and absorbing of small ellipsoid shaped nanocrystals²⁸. Considering the differences in SPR width between one- and two-photon excitation, the Gans-Mie model results in reduced peak widths of a factor $2\sqrt{\sqrt{2}-2} \approx 1.29$. Both the findings from Zijlstra and Molinaro fit with our own data, where the narrowest peaks are as narrow as 20 nm, and the broadest around 40 nm.

The location of the SPRs correspond to the absorption spectrum of the bulk solution. A sharp cut-off below 740 nm can be explained by the lower limit of the excitation wavelength at 730 nm, which impairs imaging of the plasmon peak. For wavelengths larger than 850 nm we also do not observe any SPR maxima's. We suspect this to originate from limitations in the DOE pattern by loss of focus caused by chromatic aberrations and lower laser power at these wavelengths (see Figure S2.1). Still, the resulting bandwidth of 120 nm in which we can image GNRs, is sufficient to measure the larger part of the distribution of rods considering the bulk spectrum.

The EM-CCD camera readout for single rods ranged between 15e3 and 20e3 kcounts/sec. Considering the EM-gain of 40 and the quantum efficiency of the camera, the readout signal translates to a photon count of approximately 340 to 450 photons/sec. The luminescence of GNRs is known to reach intensities of thousands of photons per second. However, reshaping of rods due to high laser intensities limits the excitation power and thereby lowering the photon emission from the rods. Nevertheless, SNR is excellent as the non-linear TPE results in an almost negligible background, dominated by readout noise of the camera.

By lowering excitation power under the damage threshold we measured stable TPE spectra. The majority of GNRs blue-shifted their SPR by a few nanometers upon initial irradiation. For these small shifts in wavelength, reshaping does not seem as the underlying mechanism as a change in aspect ratio would induce shifts of an order of magnitude larger⁶. Moreover, Zijlstra et al. showed that for rods with a plasmon resonance between 750 and 800 nm, which roughly corresponds to our distribution of measured rods, reshaping does not occur until 150 fJ of laser power is absorbed by a GNR. Reshaping below the melting temperature of gold was observed by A. Taylor et al.³⁴. They showed that their observations fitted well with a surface diffusion model from Mullins. Diffusion around the tips of the rod changes the aspect ratio causing a shift in the plasmon resonance. However, for rods with an aspect ratio between 3.8 and 4.1 – similar to the rods we use – Taylor measured a thermal threshold of approximately 60 and 40 fJ respectively. From these results, we expect that we do not see reshaping but rather that upon initial exposure to the laser beam, sedimented particles and remaining CTAB coating ($n=1.435$)⁴⁴ residing around the rods are ablated from the surface. Increasing the excitation power to above the damage threshold resulted in a linear decrease of the average SPR shift per wavelength sweep between a SPR of 800 and 740 nm. From the results of O. Ekici et al., we expect that the GNRs almost instantaneously reach thermal equilibrium when illuminated in-resonance, as there is enough time for the energy to disperse in the 12.5 ns between each femtosecond pulse of the 80 MHz pulsed laser⁴⁵. Therefore, illuminating the rods in-resonance for longer periods of time result in a linear response of the SPR shift. As the SPR is linearly dependent on the aspect ratio of the GNR, the linear decrease indicates an also linear decrease

in the aspect ratio of the rod. In the oligo-neutravidin measurements we increased laser power to slightly above the damage threshold of the GNRs, which may have resulted in a fraction of unstable rods. The difference in robustness of the GNRs to the laser illumination could arise from the uneven spatial distribution of laser intensity across the FOV or a slightly tilted excitation plane, which would reduce the absorption of a rod.

Our reference measurement for the sensitivity of the GNRs in bulk (Figure 2.5a) yielded in a sensitivity of 255 nm/RUI. This result is higher than the sensitivity of 237 ± 9 nm/RUI we measured for single GNRs in the two-photon microscope. However, differences in SPR shift between individual rods and the bulk solution are to be expected, as sensitivity to refractive index changes is highly dependent on aspect ratio and the rod-to-substrate interface^{15,46}. A lower sensitivity for individual rods when compared to bulk was also found by others, and also attributed to the physical hindrance of the substrate with the GNRs. E. Martinsson et al. studied the influence of a negatively charged glass substrate on the SPR of several differently shaped metallic nanoparticles. They measured a reduction in sensitivity of 34% when comparing GNRs in bulk and distributed on glass⁴⁷. Fortunately, we can use the multiplexed capabilities of the setup to select the most sensitive rods from the ensemble.

Additionally, our reported bulk sensitivity of 237 ± 9 nm/RUI for individual rods on a substrate, resembles the findings of other studies. M. Piliarik et al. measured a bulk sensitivity of 140 nm/RUI of GNRs with a dimension of 35 nm x 75 nm (AR = 2.14); Zijlstra et al. a bulk sensitivity of 202 ± 15 nm/RUI with an average GNR size of 37 nm x 9 nm (AR = 4.1); and Martinsson et al. found 255 nm/RUI for rods with an average size of 67 nm x 19 nm (AR = 3.5)^{15,47,48}. Differences between sensitivities are attributed to the differences in the shapes of the GNRs. The AR, absolute length and diameter of a nanorod dictates the sensitivity of a GNR for changes in the bulk refractive index, where larger rods with a larger AR have higher sensitivity^{49,50}.

Spectral studies on gold nanoparticles have been limited to scattering and photothermal microscopy. In terms of *in vivo* environments, these type of experiments are better suited for single cells or organoids. By utilizing the deep-tissue imaging capabilities of two-photon microscopy, one could envision doing spectral studies in larger animals like zebra fish embryos and mice. Besides deeper penetration depth, the low background and sensitivity of TPE would also be of considerable benefits. Sensitivity of the measurements can also be increased by making use of bipyramid-shaped nanoparticles instead of rods. Although thermally more unstable compared to rods, the more confined electrical field around the sharper tips of bipyramids, do result in a higher sensitivity to refractive index changes⁵. For addressing the thermal stability of gold nanoparticles, Y, Chen et al. found that by coating GNRs with a silica layer they were considerable more stable to pulsed laser light as when coated with CTAB or PEG⁵¹.

In our bio-sensing experiments we saw a relatively large shift of the SPR when oligo-neutravidin was added to the buffer solution, which we tentatively attributed to multiple binding events of neutravidin. To estimate how many neutravidin molecules can bind at the sensitive ends of the rods we take an average size of the rod of 40 x 40 x 10 nm³. Approximately 1/4 of the area would be blocked by the substrate. Thus a rod should have around 235 nm² exposed area. The surface area of neutravidin is approximately 22.4 nm² and thus around 10 neutravidin

molecules could bind to a rod⁵². Based on streptavidin (53 kDa) experiments by Zijlstra et al., who use similar GNRs as us, we expect a SPR shift a little over 0.5 nm per neutravidin (60 kDa) binding event⁵³. Note though that we used a DNA linker to mediate neutravidin-GNR interactions. This yields a larger distance to the GNR and hence a lower sensitivity. Ignoring this difference, a maximum number of ten neutravidin molecules per rod would therefore result in a SPR shift of 5 nm. However, some of our reported spectra feature a spectral shift of up to 20 nm, which could indicate that we measure a larger SPR shift per molecule, or that unspecific binding of impurities in the medium induces an additional red-shift. The average plasmon shift of 4 ± 1 nm of the ensemble of GNRs better matches the shift we expect. We did not observe steps in the time traces, see Figures 2.6e and S2.2d for examples. However, considering a GNR with a sensitivity of 100 photons/sec/nm, a single binding event would change the signal by 50 photons/sec, making it unlikely that the discrete steps we observed were caused by single molecule binding events. The noise on a signal with an intensity of 1019 ± 227 photons/sec, as potted in Figure 2.6e, suggests that detection of single neutravidin molecules would be hampered by a $\text{SNR} < 1$. The standard deviation of the signal however, does not correspond with the expected shot-noise of 32 photons/sec. The background noise of the camera appeared to be 99 ± 5 photons/sec (data not shown), which is excessive compared to the dark- and readout-noise of an air-cooled sCMOS camera. Other explanations might be mechanical instabilities of the microscope or temporal fluctuations in the spiral-scanning pattern. Based on the expected SPR shift and the theoretical shot-noise limit, we expect that the setup should be capable of imaging single binding events once GNRs can be imaged at shot-noise limited conditions. Another strategy to improve sensitivity would entail decreasing the linker-size between target molecule and the rod. For example, by using smaller molecules instead of oligo's, neutravidin could move closer to the surface of the rod and experience a stronger field intensity and cause a larger shift in the plasmon resonance⁵⁴.

In conclusion, we measured the TPL response on the excitation wavelength of hundreds of GNRs measured in multiplex. The narrow spectra demonstrate the possible application of two-photon microscopy with GNRs to increase the sensitivity of applications based on plasmonic nanoparticles. When ultra-high sensitivity is needed, one can decrease the peak width by almost 60% when moving from one- to two-photon excitation mechanism. Furthermore, combining high sensitivity with multi focal microscopy enables the measurement of GNRs in wide-field – allowing for acquiring statistical significant data within minutes. We demonstrated the ability of the setup to measure the change of the TPL spectra when changing the refractive index of the medium and take the first steps in single molecule bio-sensing. Given the TPL response on the refractive index and the ability to measure GNRs without reshaping, we lay a framework for TPL plasmonic single-molecule sensors.

2.5 SUPPLEMENTARY FIGURES

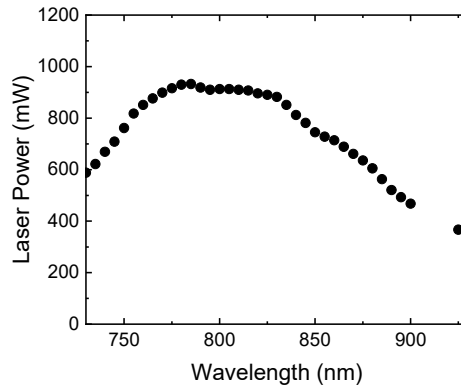


Figure S2.1: Spectrum of the maximum average laser power. Power is measured by directly placing a power meter on top of the objective.

2.5 Supplementary figures

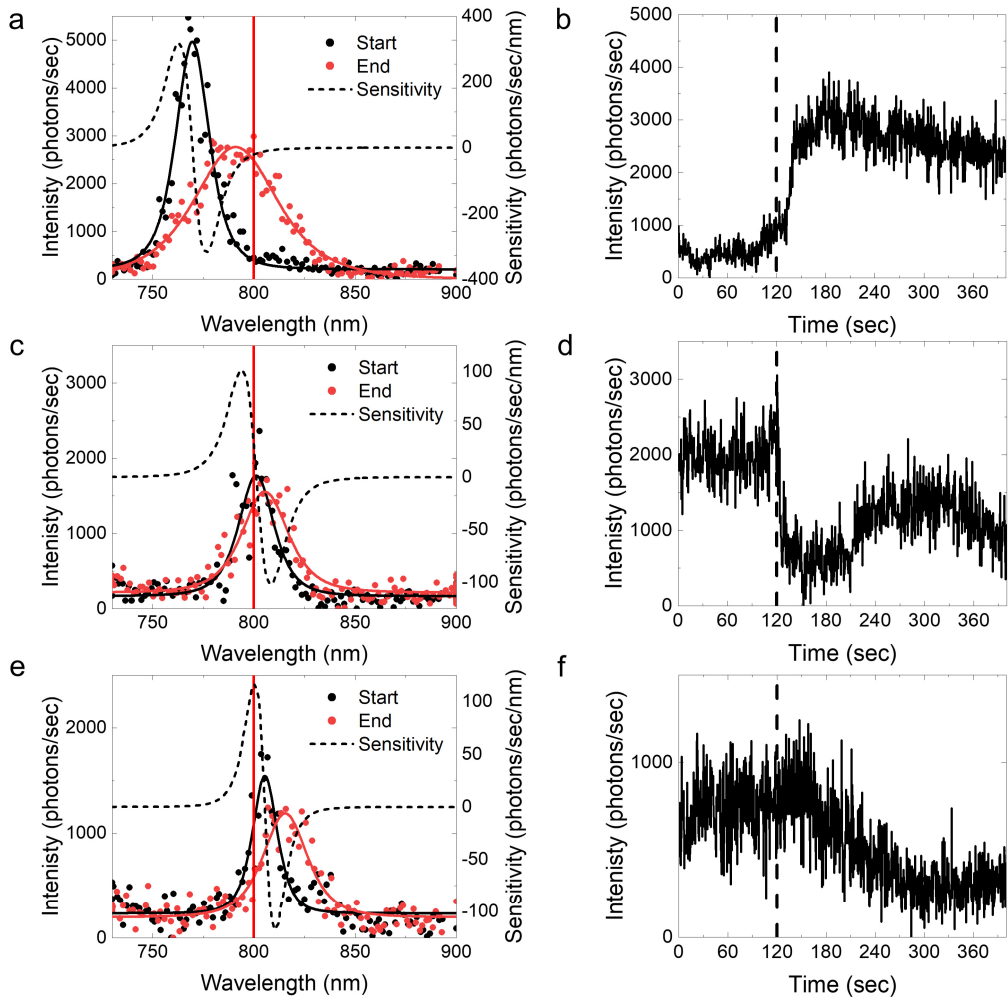


Figure S2.2: Example traces of SPR response when introducing oligo-neutravidin complexes to the surrounding medium of GNRs. (a,c,e) Excitation spectra of single gold nanorods before and after flushing in neutravidin. In all three traces there is a red-shift visible of the LSPR. (b,d,f) Time traces of the GNRs with their respective spectra on the left. Neutravidin was flushed in after 120 seconds of measuring (dotted black line), after which signal intensity starts fluctuating according to the position of the LSPR with the excitation wavelength.

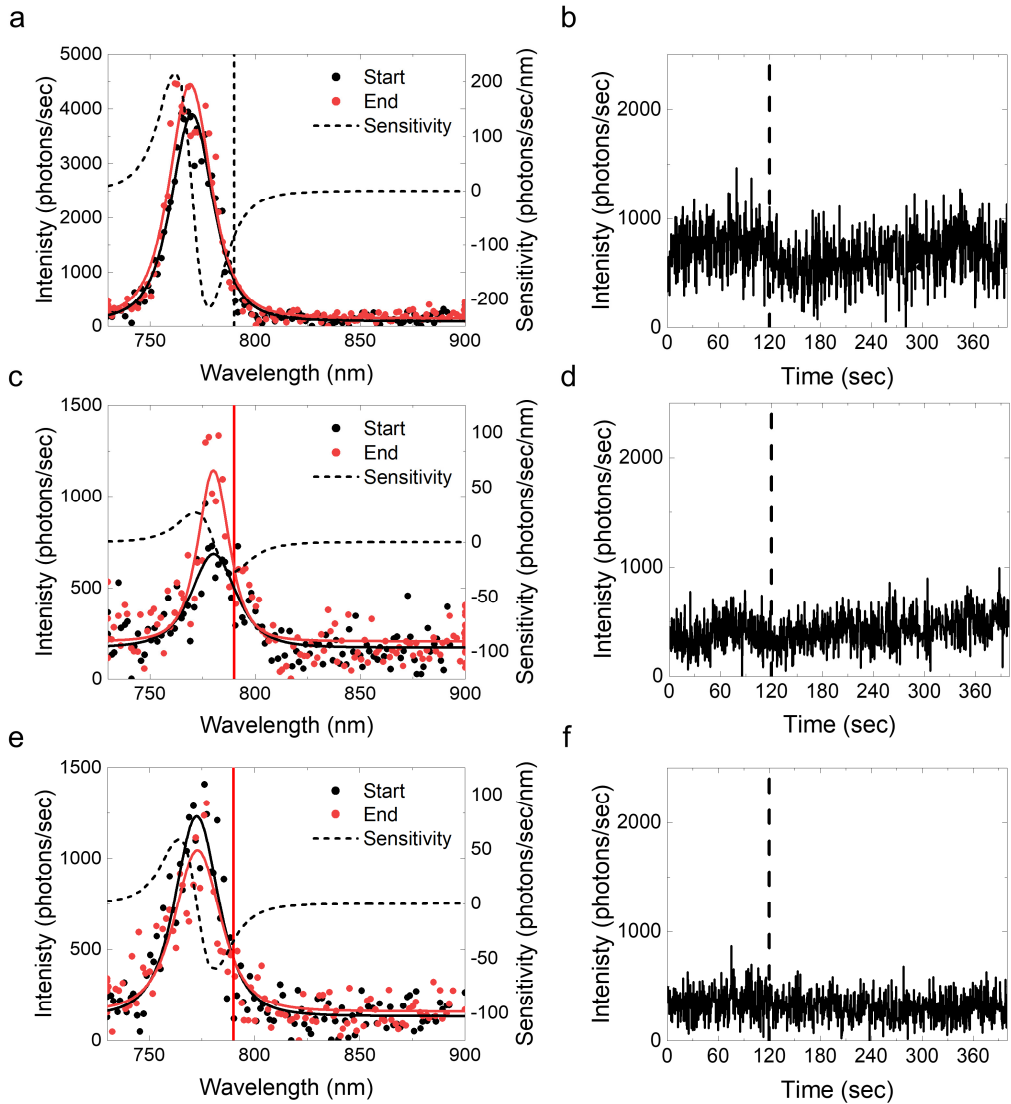


Figure S2.3: Example traces of the LSPR response of GNRs when flushing medium without oligo-neutravidin complexes in the flowcells. (a,c,e) Excitation spectra of single gold nanorods before and after the measurement. No clear LSPR shift is observed. (b,d,f) Time traces of the GNRs with their respective spectra on the left. Buffer was flushed in at 120 seconds of measuring (dotted black line), after which no significant change in signal intensity is observed.

2.6 BIBLIOGRAPHY

1. Mooradian, A. Photoluminescence of metals. *Phys. Rev. Lett.* **22**, 185–187 (1969).
2. Mohamed, M. B., Volkov, V., Link, S. & El-Sayed, M. A. The ‘lightning’ gold nanorods: Fluorescence enhancement of over a million compared to the gold metal. *Chem. Phys. Lett.* **317**, 517–523 (2000).
3. Wang, H. *et al.* In vitro and in vivo two-photon luminescence imaging of single gold nanorods. *Proc. Natl. Acad. Sci. U. S. A.* **102**, 15752–15756 (2005).
4. Van den Broek, B., Oosterkamp, T. H. & van Noort, J. A Multifocal Two-Photon Microscopy Setup for Parallel 3D Tracking of Gold Nanorods. *Biophys. J.* **98**, 178a (2010).
5. Stella M. Marinakos, Sihai Chen, and & Chilkoti*, A. Plasmonic Detection of a Model Analyte in Serum by a Gold Nanorod Sensor. (2007). doi:10.1021/AC0706527
6. Zhang, W., Caldarola, M., Pradhan, B. & Orrit, M. Gold Nanorod Enhanced Fluorescence Enables Single-Molecule Electrochemistry of Methylene Blue. *Angew. Chemie* **129**, 3620–3623 (2017).
7. Yu, C. & Irudayaraj, J. Multiplex Biosensor Using Gold Nanorods. *Anal. Chem.* **79**, 572–579 (2007).
8. Shajari, D., Bahari, A. & Gill, P. Fast and simple detection of bovine serum albumin concentration by studying its interaction with gold nanorods. *Colloids Surfaces A Physicochem. Eng. Asp.* **543**, 118–125 (2018).
9. Mohammad Eghtedari, † *et al.* High Sensitivity of In Vivo Detection of Gold Nanorods Using a Laser Optoacoustic Imaging System. *Nano Lett.* **7**, 1914–1918 (2007).
10. de la Zerda, A. *et al.* Optical coherence contrast imaging using gold nanorods in living mice eyes. *Clin. Experiment. Ophthalmol.* **43**, 358–366 (2015).
11. Ali, M. R. K., Ali, H. R., Rankin, C. R. & El-Sayed, M. A. Targeting heat shock protein 70 using gold nanorods enhances cancer cell apoptosis in low dose plasmonic photothermal therapy. *Biomaterials* **102**, 1–8 (2016).
12. Riley, R. S. & Day, E. S. Gold nanoparticle-mediated photothermal therapy: applications and opportunities for multimodal cancer treatment. *Wiley Interdiscip. Rev. Nanomedicine Nanobiotechnology* **9**, e1449 (2017).
13. Ni, W., Kou, X., Yang, Z. & Wang, J. Tailoring longitudinal surface plasmon wavelengths, scattering and absorption cross sections of gold nanorods. *ACS Nano* **2**, 677–686 (2008).
14. Nusz, G. J., Curry, A. C., Marinakos, S. M., Wax, A. & Chilkoti, A. Rational selection of gold nanorod geometry for label-free plasmonic biosensors. *ACS Nano* **3**, 795–806 (2009).
15. Zijlstra, P., Paulo, P. M. R. & Orrit, M. Optical detection of single non-absorbing

- molecules using the surface plasmon resonance of a gold nanorod. *Nat. Nanotechnol.* **7**, 379–382 (2012).
16. Ament, I., Prasad, J., Henkel, A., Schmachtel, S. & Sönnichsen, C. Single unlabeled protein detection on individual plasmonic nanoparticles. *Nano Lett.* **12**, 1092–1095 (2012).
 17. Greg J. Nusz, † *et al.* Label-Free Plasmonic Detection of Biomolecular Binding by a Single Gold Nanorod. (2008). doi:10.1021/AC7017348
 18. Taylor, A. B. & Zijlstra, P. Single-Molecule Plasmon Sensing: Current Status and Future Prospects. *ACS Sensors* **2**, 1103–1122 (2017).
 19. Beuwer, M. A., Prins, M. W. J. & Zijlstra, P. Stochastic Protein Interactions Monitored by Hundreds of Single-Molecule Plasmonic Biosensors. *Nano Lett.* **15**, 3507–3511 (2015).
 20. Olesiak-Banska, J., Waszkielewicz, M., Obstarczyk, P. & Samoc, M. Two-photon absorption and photoluminescence of colloidal gold nanoparticles and nanoclusters. *Chem. Soc. Rev.* **48**, 4087–4117 (2019).
 21. Marinakos, S. M., Chen, S. & Chilkoti, A. Plasmonic detection of a model analyte in serum by a gold nanorod sensor. *Anal. Chem.* **79**, 5278–5283 (2007).
 22. Ament, I., Prasad, J., Henkel, A., Schmachtel, S. & Sönnichsen, C. Single unlabeled protein detection on individual plasmonic nanoparticles. *Nano Lett.* **12**, 1092–1095 (2012).
 23. Wang, D.-S., Hsu, F.-Y. & Lin, C.-W. Surface plasmon effects on two photon luminescence of gold nanorods. *Opt. Express* **17**, 11350–11359 (2009).
 24. Funston, A. M., Davis, T. J., Novo, C. & Mulvaney, P. Coupling modes of gold trimer superstructures. *Phil. Trans. R. Soc. A* **369**, 3472–3482 (2011).
 25. Wackenhut, F., Failla, A. V. & Meixner, A. J. Multicolor microscopy and spectroscopy reveals the physics of the one-photon luminescence in gold nanorods. *J. Phys. Chem. C* **117**, 17870–17877 (2013).
 26. Tcherniak, A. *et al.* One-photon plasmon luminescence and its application to correlation spectroscopy as a probe for rotational and translational dynamics of gold nanorods. *J. Phys. Chem. C* **115**, 15938–15949 (2011).
 27. Zijlstra, P., Chon, J. W. M. & Gu, M. Five-dimensional optical recording mediated by surface plasmons in gold nanorods. *Nature* **459**, 410–413 (2009).
 28. Molinaro, C. *et al.* Two-Photon Luminescence of Single Colloidal Gold Nanorods: Revealing the Origin of Plasmon Relaxation in Small Nanocrystals. *J. Phys. Chem. C* **120**, 23136–23143 (2016).
 29. Ekici, O. *et al.* Thermal Analysis of Gold Nanorods Heated with Femtosecond Laser Pulses. *J. Phys. D. Appl. Phys.* **41**, 185501 (2008).
 30. Link, S. & El-Sayed, M. A. Spectroscopic determination of the melting energy of a gold nanorod. *J. Chem. Phys.* **114**, 2362–2368 (2001).

31. El-Sayed, M. A. Some Interesting Properties of Metals Confined in Time and Nanometer Space of Different Shapes. doi:10.1021/ar960016n
32. Zijlstra, P., Chon, J. W. M. & Gu, M. White light scattering spectroscopy and electron microscopy of laser induced melting in single gold nanorods. *Phys. Chem. Chem. Phys.* **11**, 5915 (2009).
33. González-Rubio, G. *et al.* Femtosecond laser reshaping yields gold nanorods with ultranarrow surface plasmon resonances. doi:10.1192/bjp.bp.108.055459
34. Taylor, A. B., Siddiquee, A. M. & Chon, J. W. M. Below melting point photothermal reshaping of single gold nanorods driven by surface diffusion. *ACS Nano* **8**, 12071–12079 (2014).
35. Gidi, Y., Bayram, S., Ablenas, C. J., Blum, A. S. & Cosa, G. Efficient One-Step PEG-Silane Passivation of Glass Surfaces for Single-Molecule Fluorescence Studies. *ACS Appl. Mater. Interfaces* **10**, 39505–39511 (2018).
36. Li, J. *et al.* Simple and Rapid Functionalization of Gold Nanorods with Oligonucleotides Using an mPEG-SH/Tween 20-Assisted Approach. doi:10.1021/acs.langmuir.5b01680
37. Funston, A. M., Davis, T. J., Novo, C. & Mulvaney, P. Coupling modes of gold trimer superstructures. *Phil. Trans. R. Soc. A* **369**, 3472–3482 (2011).
38. Garai, M., Zhang, T., Gao, N., Zhu, H. & Xu, Q.-H. Single Particle Studies on Two-Photon Photoluminescence of Gold Nanorod-Nanosphere Heterodimers. *J. Phys. Chem. C* **120**, 11621–11630 (2016).
39. Wu, J. *et al.* Angle-resolved plasmonic properties of single gold nanorod dimers. *Nano-Micro Lett.* **6**, 372–380 (2014).
40. Imura, K., Nagahara, T. & Okamoto, H. Near-field two-photon-induced photoluminescence from single gold nanorods and imaging of plasmon modes. *J. Phys. Chem. B* **109**, 13214–13220 (2005).
41. Ruijgrok, P. V., Verhart, N. R., Zijlstra, P., Tchebotareva, A. L. & Orrit, M. Brownian Fluctuations and Heating of an Optically Aligned Gold Nanorod. *Phys. Rev. Lett.* **107**, 037401 (2011).
42. and, K.-S. L. & El-Sayed*, M. A. Dependence of the Enhanced Optical Scattering Efficiency Relative to That of Absorption for Gold Metal Nanorods on Aspect Ratio, Size, End-Cap Shape, and Medium Refractive Index. (2005). doi:10.1021/JP054385P
43. Henkel, A. *et al.* Narrowing the Plasmonic Sensitivity Distribution by Considering the Individual Size of Gold Nanorods. *J. Phys. Chem. C* **122**, 10133–10137 (2018).
44. Kekicheff, P. & Spalla, O. Refractive Index of Thin Aqueous Films Confined between Two Hydrophobic Surfaces. *Langmuir* **10**, 1584–1591 (1994).
45. Ekici, O. *et al.* Thermal analysis of gold nanorods heated with femtosecond laser pulses. *J. Phys. D. Appl. Phys.* **41**, (2008).
46. Becker, J., Trügler, A., Jakab, A., Hohenester, U. & Sönnichsen, C. The Optimal Aspect Ratio of Gold Nanorods for Plasmonic Bio-sensing. *Plasmonics* **5**, 161–167 (2010).

47. Martinsson, E. *et al.* Influence of Surfactant Bilayers on the Refractive Index Sensitivity and Catalytic Properties of Anisotropic Gold Nanoparticles. *Small* **12**, 330–342 (2016).
48. Piliarik, M., Kvasnička, P., Galler, N., Krenn, J. R. & Homola, J. Local refractive index sensitivity of plasmonic nanoparticles. *Opt. Express* **19**, 9213 (2011).
49. Nusz, G. J., Curry, A. C., Marinakos, S. M., Wax, A. & Chilkoti, A. Rational selection of gold nanorod geometry for label-free plasmonic biosensors. *ACS Nano* **3**, 795–806 (2009).
50. Chen, H., Kou, X., Yang, Z., Ni, W. & Wang, J. Shape-and Size-Dependent Refractive Index Sensitivity of Gold Nanoparticles. doi:10.1021/la800305j
51. Chen, Y.-S. *et al.* Enhanced thermal stability of silica-coated gold nanorods for photoacoustic imaging and image-guided therapy. *Opt. Express* **18**, 8867–78 (2010).
52. Rosano, C., Arosio, P. & Bolognesi, M. The X-ray three-dimensional structure of avidin. *Biomol. Eng.* **16**, 5–12 (1999).
53. Zijlstra, P. & Orrit, M. Single metal nanoparticles: optical detection, spectroscopy and applications. *Reports Prog. Phys.* **74**, 106401 (2011).
54. Omair, Z. & Talukder, M. A. Sensitivity Analysis of Gold Nanorod Biosensors for Single Molecule Detection. *Plasmonics* **14**, 1611–1619 (2019).